

Quality monitoring framework for friction element welding

Original

Quality monitoring framework for friction element welding / Antal, Gabriel; Razza, Valentino; Russo Spina, Pasquale; De Maddis, Manuela. - In: JOURNAL OF MANUFACTURING PROCESSES. - ISSN 1526-6125. - Volume 156, Part A:(2025), pp. 17-28. [10.1016/j.jmapro.2025.10.083]

Availability:

This version is available at: 11583/3004787 since: 2025-11-04T09:34:59Z

Publisher:

Elsevier

Published

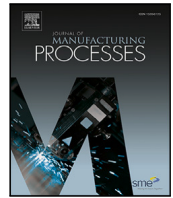
DOI:10.1016/j.jmapro.2025.10.083

Terms of use:

This article is made available under terms and conditions as specified in the corresponding bibliographic description in the repository

Publisher copyright

(Article begins on next page)



Quality monitoring framework for friction element welding[☆]

Gabriel Antal^{ID}, Valentino Razza^{ID}, Pasquale Russo Spena^{ID}, Manuela De Maddis^{ID}*

Department of Management and Production Engineering - Politecnico di Torino, Corso Duca degli Abruzzi 24, Torino, 10129, Italy
Advanced Joining Technologies Center (J-Tech@PoliTO) - Politecnico di Torino, Corso Duca degli Abruzzi 24, Torino, 10129, Italy

ARTICLE INFO

Keywords:

Friction element welding
Dissimilar metal welding
Al-steel welding
Process monitoring

ABSTRACT

The automotive industry faces challenges in reducing vehicle mass to enhance fuel efficiency and reduce gas emissions. A common strategy is to replace conventional steel body parts with thinner ultra-high-strength steels and lower-density aluminum alloys. Friction Element Welding (FEW) is a relatively recent technique developed to join these dissimilar metals in car body manufacturing.

This study presents a dedicated monitoring approach for the FEW process, designed to detect typical defects occurring in production lines. To simulate the most critical defect in automotive FEW applications, controlled initial gaps were introduced during the welding of 2000 MPa boron steel and 6xxx series aluminum alloy sheets. This approach enables the assessment of the influence of initial sheet gaps on joint quality. The results provide the basis for developing practical tools for process monitoring and quality assurance, such as control charts, validated through an experimental campaign. The findings demonstrate that the proposed method offers the potential to reduce defects and improve manufacturing efficiency.

1. Introduction

The increasing awareness of climate change has driven major transformations in many industrial sectors. In the automotive industry, manufacturers are increasingly adopting different materials to enhance the fuel efficiency of vehicles while preserving structural integrity and safety standards [1]. For instance, a 10% reduction in car body mass can lead to a decrease in fuel consumption of up to 5.5%, prompting the need for lightweight materials [2]. At the same time, cost-efficient and scalable technologies remain essential. Aluminum alloys have emerged as promising substitutes for specific steel components, and suitable joining techniques are critical to their successful integration [3].

Resistance spot welding (RSW), the leading joining technique in the automotive sector, faces several limitations when welding dissimilar metal grades. Aluminum-to-steel welds present challenges due to differences in contact and bulk electrical resistance, thermal conductivity, and melting point. Moreover, the formation of detrimental Fe-Al intermetallic compounds (IMCs) can significantly degrade joint quality [4]. In response, researchers have proposed various process enhancements. For instance, Ding et al. [5] embedded a linear actuator into the electrodes to better regulate and control the clamping force, thereby improving the quality of the aluminum nugget. Similarly, Shi et al. [6] successfully employed multi-ring domed electrodes and multistage solidification schedules to produce Al-steel spot welds.

To address the shortcomings of RSW in welding aluminum to steel, a solution involves employing mechanical joining methods, such as self-piercing riveting (SPR), in which a semi-tubular rivet penetrates the top sheet and expands into the bottom sheet using a die, which plastically deforms the lower material to form a mechanical interlock. However, ultra-high strength steel (UHSS) and low ductility materials pose significant challenges for the SPR process [7], although a recent study shows promising results [8]. Hybrid solutions have been developed to overcome the limitations of traditional mechanical joining techniques arising from the introduction of advanced and hard-to-weld materials, such as UHSS. These include Resistance Element Welding (REW), Resistance Rivet Welding (RRW), and Friction Element Welding (FEW). These processes are particularly well-suited for automotive applications. REW involves two stages: in the first stage, a rivet-like element, serving as an auxiliary joining component and made from a material compatible with the upper sheet (e.g., aluminum), is punched into the upper material layer. In the second stage, this element is resistance spot-welded to the lower sheet steel, completing the joint [2, 3]. In contrast, RRW eliminates the need for a pre-insertion of the rivet in the upper sheet, potentially reducing both processing time and costs [9,10]. The main advantage of both REW and RRW is their compatibility with existing RSW equipment, enabling manufacturers

[☆] This article is part of a Special issue entitled: ‘Trends on spot joining’ published in Journal of Manufacturing Processes.

* Correspondence to: Politecnico di Torino, Corso Duca degli Abruzzi 24, Torino, 10129, Italy.

E-mail addresses: gabriel.antal@polito.it (G. Antal), valentino.razza@polito.it (V. Razza), pasquale.russospena@polito.it (P. Russo Spena), manuela.demaddis@polito.it (M. De Maddis).

<https://doi.org/10.1016/j.jmapro.2025.10.083>

Received 9 July 2025; Received in revised form 14 October 2025; Accepted 27 October 2025

1526-6125/© 2025 The Authors. Published by Elsevier Ltd on behalf of The Society of Manufacturing Engineers. This is an open access article under the CC BY-NC-ND license (<http://creativecommons.org/licenses/by-nc-nd/4.0/>).

to reconfigure and retrofit current infrastructure, achieving significant cost savings [11,12]. Conversely, FEW uses a high-speed rotating (often over 3000 rpm) element (also called rivet) that penetrates the upper sheet and welds to the lower sheet through frictional heat and a high axial force (5-10 kN) [1]. FEW shares some similarities with Friction Riveting (FR), as both are solid-state joining techniques that generate and use frictional heat to create a bond. However, they differ markedly in their operating principles, the materials they join, and the nature of the resulting joint. In FR, a cylindrical metallic rivet is rotated at high speed and driven into a polymer or fiber-reinforced composite component, often in combination with a metal sheet. The frictional heat generated at the interface softens the rivet tip, which plastically deforms and anchors within the polymer matrix. This results in a mechanical–thermal interlock rather than a fully metallurgical bond between dissimilar materials, making the technique particularly suitable for aerospace, marine, and automotive applications that incorporate hybrid structures. FEW, by contrast, is intended primarily for metal-to-metal joining using a metallic element similar in appearance to a rivet or fastener [13]. Although FEW requires specific equipment, it offers several notable advantages over the other welding technologies: lower processing temperatures (i.e., no melting of sheets), elimination or reduced formation of Al-Fe IMCs, and higher joint strength when employing the same material combination [1,12].

Despite being a relatively new joining technique, FEW has been the subject of increasing research. Meschut et al. [14] investigated process optimization and the influence of zinc-based anticorrosive coatings. Skovron et al. [15] assessed the impact of various welding parameters on key performance indicators, e.g., welding time, energy consumption, temperature, torque, element head height, weld diameter, and under-head filling. Their findings indicate that the cleaning step had the most significant influence on both processing time and energy consumption, while element head displacement is the primary factor affecting head height and underhead filling. Torque is influenced by both axial force and the displacement of the element. Ruzkiewicz et al. [16] examined the sensitivity of welding parameters to minimize processing time while maintaining adequate joint mechanical performance. Other studies have primarily focused on reducing processing time. Awate et al. [17] studied the effect of the addition of SiC abrasive particles in the weld region. They reported both reduced processing time and improved joint strength. Deshpande et al. [18] demonstrated that thermal assistance can help reduce chipping and shorten processing durations. Specifically, the authors used a furnace to heat the aluminum cover sheet. Five different temperature levels, ranging from 20 °C to 427 °C, were investigated. Other studies have confirmed the benefits of additional heating, achieved through laser beams [19] or electrical currents [20], during the FEW process. Modeling and simulation efforts have provided deeper insights into the FEW process. Varma et al. investigated material deformation, temperature evolution [21], and the chipping phenomenon during welding [22]. Absar et al. [23] proposed the use of micro thin-film thermocouples throughout the weld region for precise temperature monitoring, which is essential to validate numerical models.

With the advent of Industry 4.0, new tools for real-time quality assessment of welding processes and assemblies are emerging and becoming increasingly important [24]. However, to the best of the authors' knowledge, no previous studies have specifically addressed monitoring in the FEW process. Pre-existing gaps in sheet stacks are the major factor affecting the quality and performance of FEW joints. Such gaps typically result from imperfect sheet matching, induced by non-ideal geometries and residual deformations accumulated during prior manufacturing and/or joining operations. Their presence prevents proper contact between sheets, leading to insufficient under-head filling, incomplete metallurgical bonding, excessive protrusion of the element head, and smaller welded areas. Although optimization of process parameters can mitigate or eliminate some of these shortcomings, it cannot eliminate the formation of peripheral gaps surrounding the

joint, as they are a direct consequence of the initial sheet gap. Indeed, while the element locally succeeds in squeezing the sheets together, it leaves a peripheral gap surrounding the joint that remains after the FEW process. This defect, by far the most recurrent automotive FEW assembled parts, can compromise the load-bearing capacity and weld reliability. Even minor misalignments or uneven surfaces can introduce variability in the welding process, making it difficult to achieve repeatable high-strength joints. Therefore, understanding and controlling the influence of pre-existing gaps is essential for ensuring the structural integrity and performance of FEW assemblies, especially in demanding applications such as automotive body structures.

This work proposes a quality monitoring framework for the FEW process. The approach begins with a thorough process analysis and the definition of quality requirements. Following process optimization and sensor system integration, an experimental campaign has been conducted to investigate the effect of pre-existing sheet gaps. These gaps are intentionally introduced during the welding of 2000 MPa boron steel to a 6xxx-series aluminum alloy, a promising material combination for lightweight and high-strength automotive body structures with improved crashworthiness. During welding, key process signals, such as axial force (i.e., vertical force applied by the element) and element displacement, are recorded, along with the temperature captured around the welded joint using a thermal camera and thermocouples. While temperature measurements provide valuable insights into joint quality, their implementation in large-scale production could be prohibitive. Therefore, the study investigates correlations between thermal data and readily available process signals to identify practical monitoring features. Based on the collected data, control charts are developed as practical tools for process monitoring and defect detection.

2. Methodology

This chapter describes the methodology applied in this study, as illustrated in Fig. 1. The approach is structured into four main stages. The first stage, *Process overview*, involves an in-depth analysis of the FEW process and the identification of relevant quality requirements. The second stage, *Experimental phase*, concerns the implementation of the sensor system and the execution of the experimental welding campaign. The third stage, *Data analysis*, deals with the selection and extraction of engineering features from process signals. Based on this analysis, a feedback loop to the second stage, referred to as *Sensor selection*, may occur if some sensors are deemed to be unnecessary and subsequently removed. The final stage, *Decision support tool development and testing*, involves the development and testing of the decision support tool (DST). Depending on the DST performance, it may be necessary to return to the third stage to select additional features. All the main stages, along with their relative sub-stages applied to the FEW process, are discussed in detail in this chapter.

2.1. Process overview

This stage includes 2 sub-stages: the process analysis and the quality criteria specification. During FEW, a rotating steel element penetrates the upper aluminum sheet under axial force, softening the material through frictional heat and forming a strong weld with the bottom steel sheet. The process shown in Fig. 2 consists of four sequential phases:

- **Penetration:** the rotating element is forced through the upper aluminum sheet by an axial force. As it advances through this sheet, friction generates heat, softening the aluminum and causing it to undergo plastic deformation. The material flows around the element shaft and beneath its head.
- **Cleaning:** once the element tip makes contact with the surface of the bottom steel sheet, friction increases significantly due to the higher strength of the steel. The resulting temperature rise plastically deforms the element tip, causing it to upset and

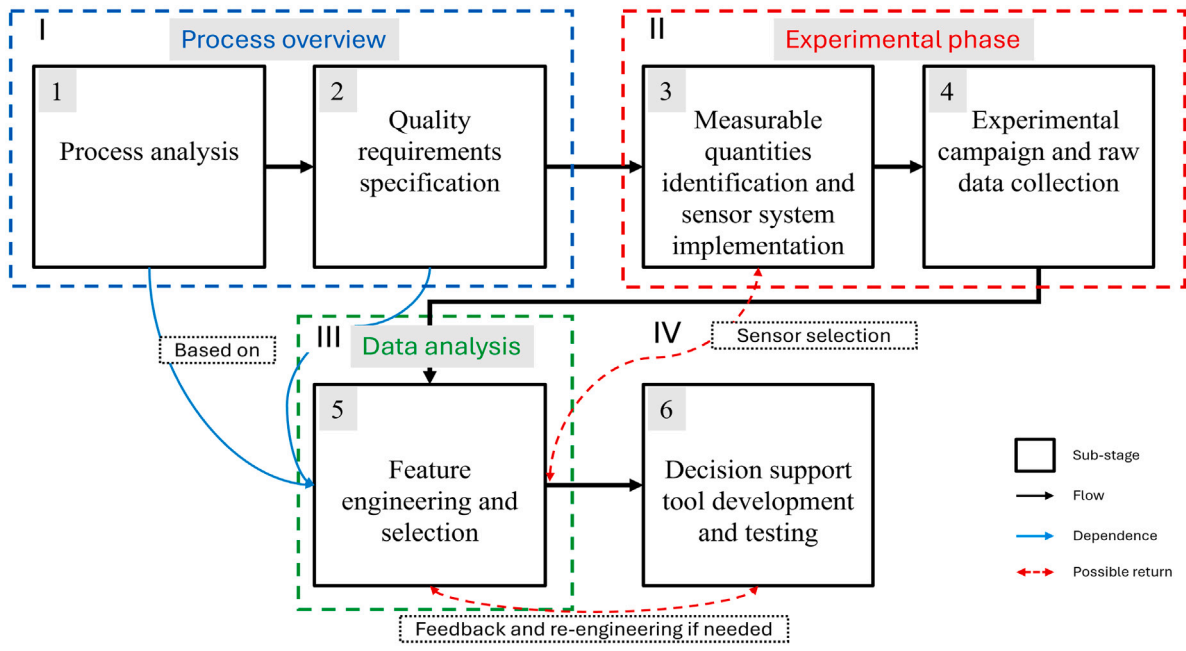


Fig. 1. Methodology adopted for the quality monitoring framework for FEW.

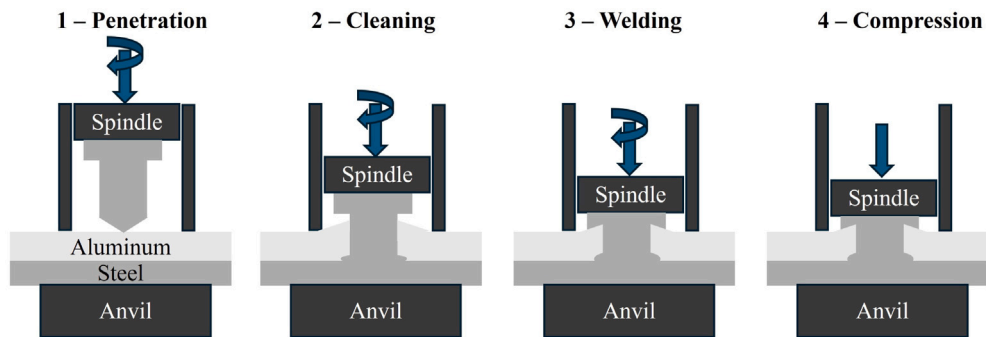


Fig. 2. FEW schematization.

spread laterally, forming a characteristic upset around the shaft. Although the steel sheet itself does not deform significantly, its surface is effectively cleaned, and any anticorrosion coatings are removed. This phase demands more time and energy than the others, but it is critical to the overall process: the heat generated through friction lowers steel resistance to deformation, effectively preparing the materials for the subsequent welding phase. This ensures proper metallurgical bonding between the element and the steel sheet, and hence plays a key role in determining the final quality of the joint.

- **Welding:** continued frictional interaction leads to the formation of a solid-state weld between the element and the steel sheet. The element undergoes further plastic deformation and is progressively upset into the aluminum sheet, completing the mechanical interlock.
- **Compression:** the element rotation is stopped, and a final higher axial force is applied. This step closes any cracks that may have formed during deceleration and ensures the element head is firmly embedded in the aluminum sheet, finalizing the joint.

The main input parameters governing all phases of the FEW process are: (i) axial force, (ii) element rotational speed, and (iii) element head displacement. Among these, head displacement (set at 0 at the onset of the penetration phase) controls the transitions between penetration,

cleaning, and welding phases: each of these phases ends once a pre-defined head displacement value (set by the operator) is reached. In contrast, the compression phase is time-controlled, with its duration also set by the operator.

The quality of FEW joints is assessed based on several geometrical and microstructural features, as highlighted in Fig. 3. A welded joint meets the quality requirements when these features fall within specific limits and fulfill defined conditions. The quality requirements used in this study, as reported in Table 1, were defined according to established automotive recommendations [25] for a stack of 2 mm-thick Al and steel sheets.

2.2. Experimental phase

The experimental stage consisted of the sensor system implementation and data collection to describe both the behavior of the reference (i.e., benchmark) and the disturbed processes.

A preliminary welding campaign was conducted to evaluate the performance of the welding machine and sensors, define the benchmark process, and verify and validate the selected quality requirements.

The objective was to define a reference process (i.e., benchmark) that consistently produced joint samples meeting all quality requirements shown in Table 1. Additionally, the joining process had to be the

Table 1

Quality requirement specifications for FEW welds [25]. They refer to 2 mm-thick Al and steel sheets and a CFF® element.

Joint quality factors	Motivation and requirement
Chip formation	Chips around the element head can compromise the bodywork and its corrosion resistance. <i>Requirement: Absence of chips around the element head.</i>
Under-head filling	Under-head filling affects the joint impermeability. <i>Requirement: Contact length between the upper sheet and the area under the element head, L_F, greater than half of the under-head length, L_H, ($L_F \geq \frac{1}{2} L_H$).</i>
Excess element head	The height of the element head, E , must be experimentally determined based on sheet characteristics and thickness. <i>Requirement: 2.8 – 3.2 mm.</i>
Head angle	The head inclination angle indicates a possible incorrect robot positioning and affects joint quality. <i>Requirement: If $\theta > 3^\circ$, equipment inspection is necessary.</i>
Welded zone diameter	The welded zone diameter is essential for joint quality and must be larger than the element stem diameter (4.55 mm). <i>Requirement: $\varnothing_{\text{welded zone}} > \varnothing_{\text{element stem}}$.</i>
Cracks in the welded zone	Cracks in the welding zone can compromise joint strength. <i>Requirement: Crack length < 0.5 mm</i>
Wrinkles in the welded zone	Wrinkles are local surface deformations that can appear in the element or the surrounding material during the welding process. They usually occur when the element is excessively compressed since the material is forced to deform plastically, leading to the formation of wrinkles. <i>Requirement: Wrinkles have to be located outside a cylindrical region of 3.5 mm in diameter centered on the element axis</i>
Post-welding gap	The sheet gap surrounding the FEW joint is caused by imperfect matching between the sheets to be assembled. It is measured at 8 mm from the element axis (in both directions). <i>Requirement: gap ≤ 0.5 mm</i>

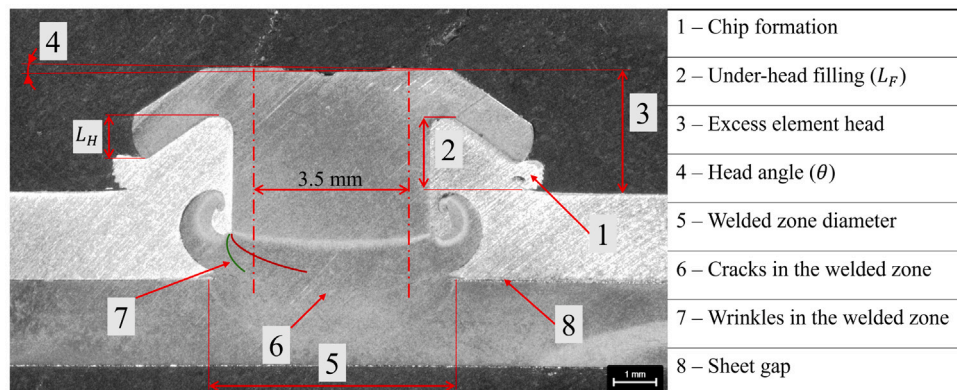


Fig. 3. Example of an aluminum-steel joint and typical quality requirements. Each number indicates the potential defect location to be checked.

right tradeoff between joint strength, which generally increases with welding time, and energy consumption.

The experimental setup for the FEW test is shown in Fig. 4. FEW was carried out using a second-generation EJOWELD® machine. This machine used built-in sensors, which operated at a sampling frequency of 500 Hz, to monitor several process parameters (energy consumption, process time, element head movement, rotational element speed, and so forth). The element used was made with a boron steel and had a CFF® geometry, with a shaft diameter of 4.55 mm and a total height of 7.20 mm (more details can be found in [26]). The upper sheet was a 6xxx series aluminum alloy, while the lower sheet was an ultra-high strength 37MnB4 steel (trade name Usibor® 2000). Both sheets were 2 mm thick.

Since the joining process can be stopped after the penetration and cleaning phases, the reference process was determined by incrementally optimizing the input parameters for each stage (i.e., first for penetration, then for both penetration and cleaning, and finally for

the full sequence). As previously discussed, the input parameters are the axial force, F , element rotational speed, n , and element head displacement, s , in the first three phases. The machine advances to the next phase once the set displacement is reached. In contrast, the final compression is time-controlled as follows: 9 kN load for 300 ms without element rotation. Preliminary tests confirmed the suitability of this setting, validating their direct adoption in the process without further adjustment.

During the penetration phase, the main focus was on minimizing chip formation, as it compromises the corrosion resistance of the joint. After cleaning, the requirement was the welding zone diameter. A chisel test verified whether this diameter exceeded that of the element shaft (i.e., 4.55 mm). The welding and final compression stages were defined to produce joints that fulfilled all the quality requirements in Table 1, which were verified through metallographic examination (see Fig. 3).

Ultimately, three configurations that satisfied all geometrical quality specifications (Table 1) were selected. The selection was made

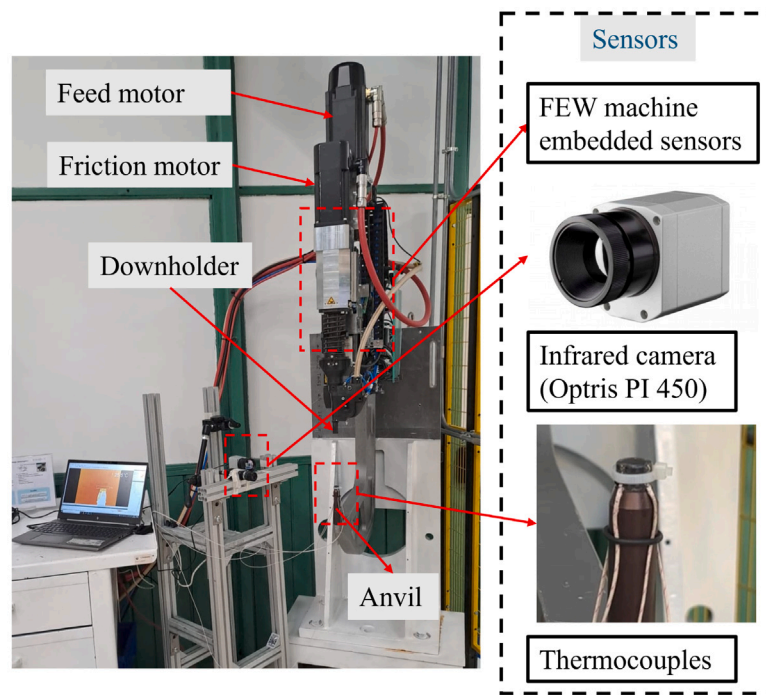


Fig. 4. Experimental setup. The main components and sensors are highlighted.

Table 2

Benchmark process input parameters. Element head displacement (s), axial force (F), and rotational speed (n) are reported.

Parameter	Penetration	Cleaning	Welding	Compression
s (mm)	1.8	2.8	4.0	
F (kN)	8	5	5	9 kN for 300 ms ^a
n (rpm)	4000	7000	7000	

^a FEW element does not rotate during the Compression phase.

because their energy consumption and process time could be broadly categorized into high, intermediate, and low levels of energy consumption and process time, thus providing a representative spectrum of operating conditions (mean and standard deviation computed on 5 samples): Case (i) 3468.5 ± 159.0 W s and 2.48 ± 0.13 s (high energy consumption and process time), Case (ii) 3161 ± 304.0 W s and 2.36 ± 0.19 s (intermediate energy consumption and process time), Case (iii) 2687.4 ± 103.1 W s and 1.99 ± 0.05 s (low energy consumption and process time). Shear tension tests were carried out on the same five samples for each configuration (sample size Al 110x50 mm, Usibor 100x50 mm, overlap 20 mm) to evaluate joint strength. The peak load obtained was, respectively, 9.42 ± 0.46 kN, 8.18 ± 0.94 kN, and 7.52 ± 1.57 kN. Although all three configurations meet the minimum requirements outlined in Table 1, Case (i) provides the highest mechanical strength along with the lowest variability. Such performance is particularly desirable in a production environment, as it ensures a consistently high standard of quality. For this reason, this configuration was selected as the benchmark process. The corresponding input parameters for phases 1–3 are detailed in Table 2. It is worth noting that further studies could be aimed at reducing energy consumption and process time while maintaining adequate weld strength, as exemplified by Case (ii). Instead, Case (iii) suffers from a low shear tension strength and high variability, which makes this configuration unsuitable for automotive standards.

Once the benchmark process was completed, the next stage involved identifying the measurable physical quantities relevant to the joining process and the corresponding sensors, as described in Table 3. These variables were measured using the FEW machine built-in sensors. Since the joint could not be measured directly, as it was firmly clamped

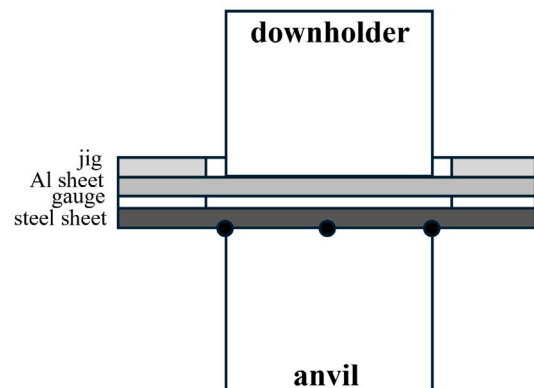


Fig. 5. Initial gap (IG) configuration, with $IG = \{0.2, 0.3, 0.4, 0.5, 0.6, 1.3, 1.5, 1.9\}$ mm. The black points indicate the thermocouples positions.

between the anvil and the downholder (see Fig. 2), the temperature around the weld area was measured using an Optris PI 450 IR thermal camera and a set of thermocouples.

The thermal camera captured thermal images at a resolution of 382×288 px (pixel), with a spatial resolution of about 0.24 mm/px (i.e., only defects larger than 0.24 mm can be potentially detected) at 30 fps. The temperature data from the IR camera were limited to a defined region of interest (ROI). A linear ROI was positioned along the vertical axis of the FEW machine to ensure relevant and

Table 3
Measurable physical quantities during FEW experiments.

Symbol	Unit	Description
E	(Ws)	Energy consumption during the process phases
t	(s)	Total process duration
F	(kN)	Axial force
s	(mm)	Element head displacement
IFM	(%)	Friction motor power (percentage of the max value)
IF	(%)	Feed motor power (percentage of the max value)
n	(rpm)	Friction motor speed
M	(Nm)	Friction motor torque
T	(°C)	Welding area temperature

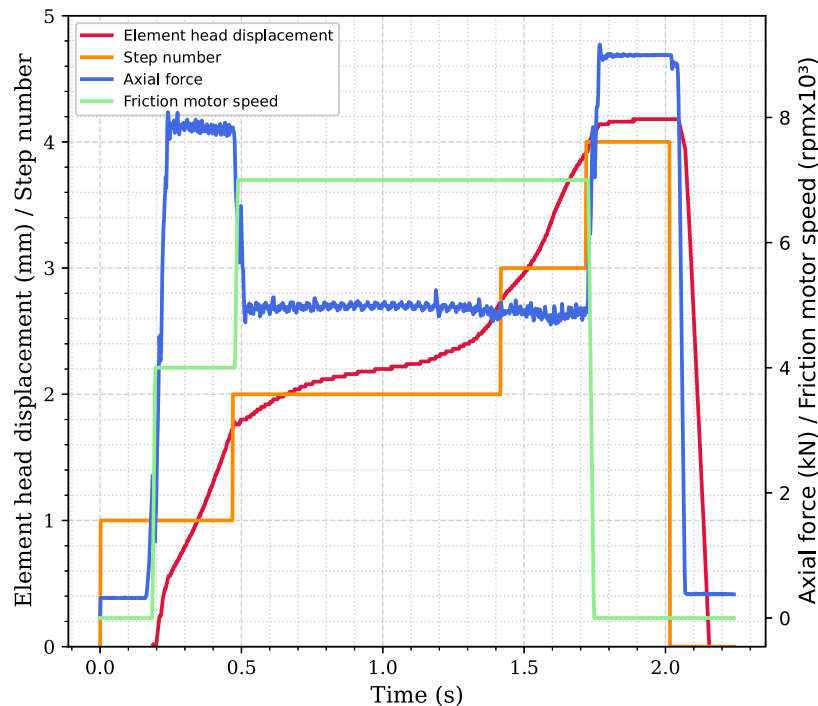


Fig. 6. Examples of the process signals from a sheet sample obtained with the benchmark parameters (IG0).

consistent data acquisition. As illustrated in Fig. 5, a custom jig was designed to precisely center the weld within each sample, enhancing the repeatability and reliability of temperature measurements. It was made by a 40x40x2 mm aluminum sheet that, during the experiment, was placed upon the sheet stack. Four glass fiber thermocouples (3 mm in diameter and suitable for temperature measurements up to 400 °C) were attached to the lower steel sheet along a circular path at the anvil exit to measure the temperature in proximity of the weld area during the joining process. They were positioned at angular intervals of 90°, ensuring an equidistant distribution along the measurement circle (refer to Figs. 4 and 5). Data acquisition, at a sampling frequency of 1 kHz, was handled using a National Instruments NI-USB 6211 DAQ board, paired with custom LabVIEW software.

The last sub-stage involves experimental work, including numerous welding tests and the acquisition of data for both the nominal process and conditions with intentionally introduced defects. It consists of two steps: (i) the production of samples using the previously defined benchmark process, and (ii) the simulation of gap defects. With the benchmark process established, the next step was to artificially reproduce the most common defect observed in FEW of automotive sheets: the gap between the two welded sheets surrounding the joint. As mentioned previously, such gaps originate primarily from poor initial matching of the sheets before welding. As presented in Table 1, the post-weld gap was measured at a distance of 8 mm from the joint

axis, with the maximum allowed value at this location not exceeding 0.5 mm.

To artificially reproduce the defect, an initial gap (IG) was introduced on both sides of the joint region by inserting calibrated thickness gauges. The configuration of the sheet stack along with the gauges and the jig is displayed in Fig. 5. A range of IG values was selected - {0.2, 0.3, 0.4, 0.5, 0.6, 1.3, 1.5, 1.9} mm - to progressively assess the effect of increasing IG size on the resulting post-weld gaps. The post-welding gaps were measured through cross-sectional analysis of the FEW joints. All samples with induced IG were welded using the previously defined benchmark parameters.

2.3. Data analysis

Based on process characteristics, signal features indicative of gap conditions were investigated through the analysis of the FEW machine data. The goal was to identify signal features that can reliably indicate the presence of anomalies while exhibiting low variability under the benchmark process condition (i.e., when the process is under control). This task is part of the broader data analysis stage. Other sub-stages, such as data preprocessing, are beyond the scope of this discussion and are therefore not included in Fig. 1. As shown in the figure, feature engineering is based on both process analysis and quality requirements. For example, in the presence of a gap, changes in the final head position

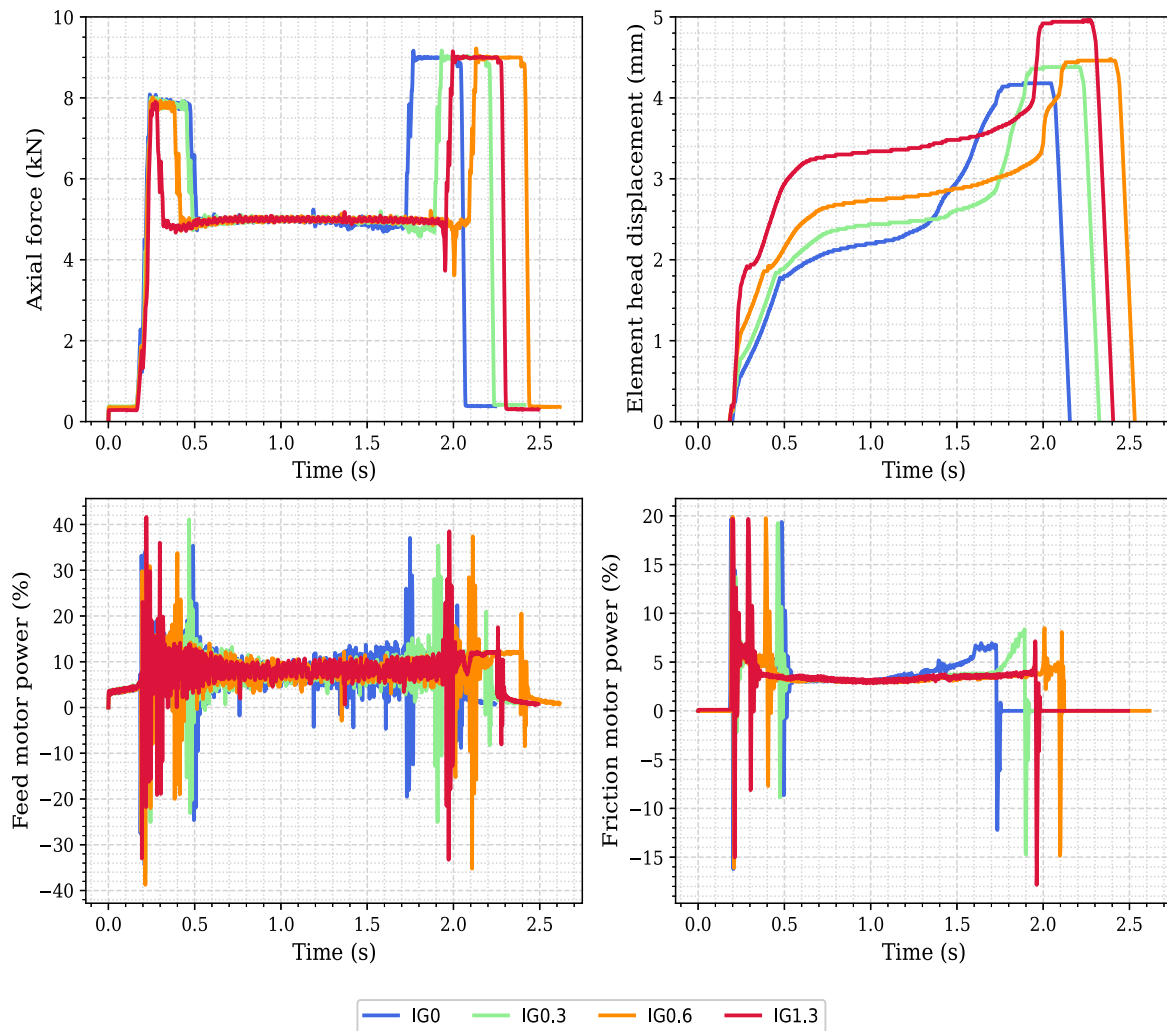


Fig. 7. Axial force, element head displacement, feed motor power, and friction motor power signals obtained from different initial gaps. IG0 corresponds to the benchmark process.

are expected since most phases of the FEW process are controlled by element head displacement (see Table 3).

2.3.1. Benchmark process signals analysis

Before feature extractions, the behavior of the benchmark process was first analyzed. Fig. 6 shows the time evolution of element head displacement, step number, axial force, and element rotational speed for a representative sample processed under the benchmark condition. As previously mentioned, the duration, and hence the transitions, between the first three process phases are driven by head displacement: when the head reaches a predefined displacement (see Table 2), the process moves to the next phase. At the same time, both rotational speed and axial force are adjusted to preset values. The slope of the displacement curve provides further insights into process dynamics. In the first phase, the element penetration speed is high due to the low mechanical strength of aluminum. However, during the subsequent cleaning phase (displacement range of 1.8–2.8 mm), the dynamics change notably. Element deceleration occurs for two reasons: a reduction in axial force and the contact between the element and the steel sheet. This cleaning phase is crucial in the FEW process, as adequate heat generated through friction reduces the steel resistance to deformation, thereby preparing the materials for the welding phase. As a result, the slope of the displacement curve increases despite the same axial force (5 kN) and a higher head displacement (1.2 mm, from 2.8 mm to 4 mm).

Based on a dataset of 25 specimens, samples processed under the benchmark condition exhibit consistent process signals, with an average total process time of 2.46 ± 0.14 s.

2.3.2. Gap process signals analysis

The axial force, element head displacement, and motors power signals from specimens with different initial gaps, $IG = \{0.3, 0.6, 1.3\}$, are compared to the benchmark case ($IG = 0$), as shown in Fig. 6. Other measurable physical quantities reported in Table 3 were not considered in the data analysis: energy consumption (proportional to process time) and friction motor torque (proportional to motor power since element rotational speed is constant in each phase).

Regarding the axial force during the penetration phase ($F = 8$ kN), it can be observed that the duration of this phase shortens as IG increases. This effect is especially pronounced with IG1.3 (red curve in Fig. 7 top left). Two main reasons contribute to this behavior: (i) the transition to the cleaning phase is triggered at a fixed head displacement of 1.8 mm, and (ii) the presence of a gap reduces material resistance to penetration, leading to a faster advancement of the element. This trend is also confirmed by the head displacement curves (Fig. 7, top right), where the slope between 0 and 1.8 mm becomes steeper as IG increases, indicating higher velocity in reaching the preset head displacement.

A similar pattern is observed during the cleaning phase: larger IGs result in steeper displacement curves and shorter phase durations.

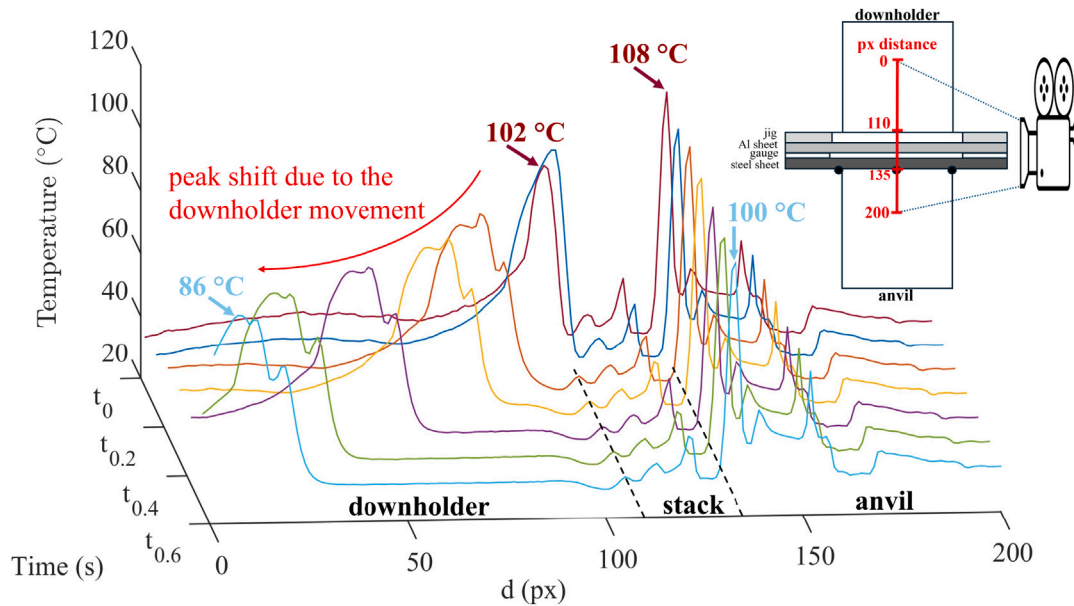


Fig. 8. Example of the temperature distribution along the linear ROI. Each curve corresponds to a specific time instant, ranging from $t = 0$ s (onset of the downholder upward motion) to $t = 0.6$ s. The schematic in the top-right corner (not to scale) illustrates the ROI together with selected characteristic pixel distances (1 px = 0.24 mm).

Conversely, the welding phase (range 2.8–4 mm) is much longer for larger IG values. This is attributed to insufficient frictional heat generated during a short cleaning phase, which impairs the achievement of adequate welding temperatures. As a result, the welding phase requires more time to achieve the target head displacement of 4 mm, which reflects in a lower slope of the displacement curve. Interestingly, the total duration of all three phases (i.e., penetration + cleaning + welding) remains approximately constant at varying IGs. All gap-affected welding durations fall within the time range of the benchmark condition (2.46 ± 0.14 s), indicating that total process time alone is not a reliable indicator of the presence of an initial gap between sheets. However, final displacement values tend to be higher for larger IGs. During the final compression phase ($F = 9$ kN for 300 ms), the longer welding phase allows deeper element penetration, resulting in greater overall head displacement. Similar considerations also apply to the two power signals, which exhibit comparable profiles and pronounced peaks at process phase transitions, occurring when the element head reaches the preset travel distance.

In conclusion, while all samples share the same displacement target, the rate at which this displacement is achieved varies with the initial gap. Therefore, time-based features, such as phase durations and displacement curve slopes, are more effective for identifying both the presence and severity of an initial gap between sheets.

2.3.3. Temperature signals analysis

Temperature measurements were acquired for samples with IG of {0, 0.2, 0.3, 0.4, 0.5, 0.6} mm. Some limitations must be acknowledged regarding the use of thermocouples and an IR camera for temperature measurements. Thermocouples, when properly installed, provide accurate pointwise measurements; however, they suffer from several disadvantages, including sensitivity to positioning errors, wear degradation, and uncorrect measurements due to machine vibrations, and considerable challenges related to installation in industrial environments. Conversely, thermal imaging offers a more practical and robust approach for process monitoring, as it provides comprehensive spatial information with lower sensitivity to mechanical wear and alignment errors. Nevertheless, this technique cannot directly capture the temperature at the joint, since it is enclosed between the downholder and the anvil. With the thermal camera positioned perpendicular to

the vertical axis of the machine, it recorded the temperature of the anvil and downholder surfaces close to the sheet stack and the edge of the sheet stack. Despite this limitation, the temperature evolution in these regions, along the ROI, can offer valuable indirect insights into the thermal behavior during the welding process. Fig. 8 shows an example of the temperature profile acquired during a single experiment along the ROI at the end of the welding process (set as $t_0 = 0$ s), corresponding to the onset of the upward motion of the downholder as it released the welded sample. The ROI was oriented along a linear path, aligned to the axis machine, extending from the downholder to the anvil through the sheet stack (top-right side in Fig. 8). The thermal camera captured a recurring “bell-shaped” temperature profile. The first part of the curves progressively shifts left (i.e., toward lower distance values) over time, corresponding to the opening movement of the downholder as it releases the welded sample. Each curve displays two distinct temperature peaks, one located on the anvil and the other on the downholder. For example, the instant $t = 0$ s shows the peak temperature (102 °C) recorded on the downholder surface close to the sheet stack (at 108 px distance). Beneath this region lies a 20–30 pixel-wide zone at near-ambient temperature corresponding to the border of the sheet stack, followed by a second peak of 108 °C.

After 0.6 s, the two temperature peaks decreased to 86 °C and 100 °C, respectively. The temperature reduction was less pronounced for the anvil because the welded sample remained in contact with it, whereas the downholder detached and moved upward. These observations suggest that the heat generated during the FEW process did not propagate to the sample edges (20 mm away from the weld center) within the short welding duration (~ 2 s).

Fig. 9 compares IR camera and thermocouple measurements for IG0, IG0.3, and IG0.6 over a 4 s time interval, starting from the onset of the temperature rise (taken as the process start point). The IR camera measurements correspond to the pixel on the upper side of the anvil closest to the sheet stack, thereby enabling the most direct possible comparison of the temperature data obtained from the same region. Peak temperatures were typically achieved at around 2 s, in correspondence with the end of the welding process.

Fig. 9 shows that the thermocouples may exhibit segments of the temperature profile with inconsistent values, as observed in the case of IG0 and IG0.4, where the measured temperature abruptly decreases

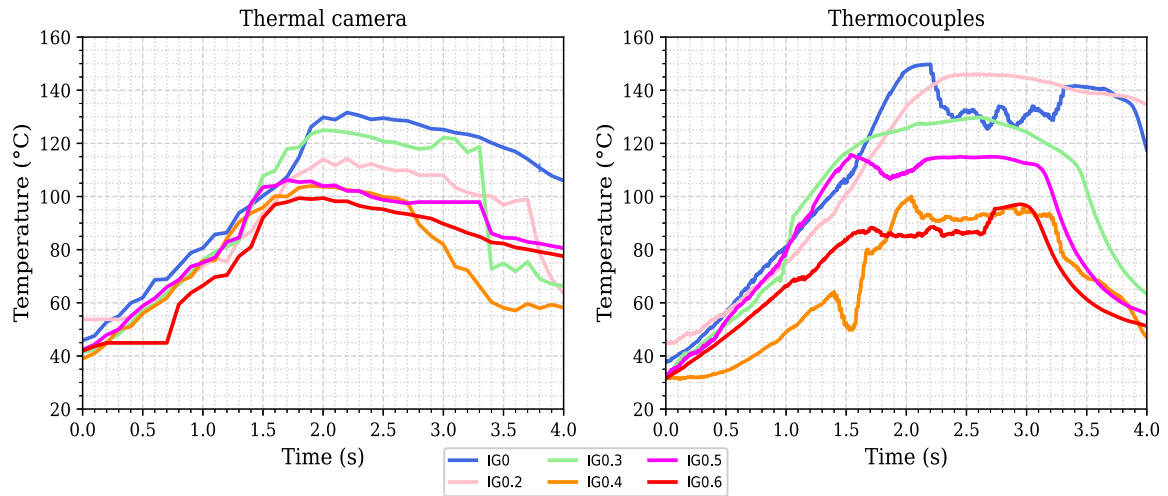


Fig. 9. Comparison of temperatures measured by the thermal camera (pixel on the anvil closest to the sheet stack) and by thermocouples during welding tests at varying IGs. IG0 corresponds to the benchmark process.

Post-process gap correlation matrix

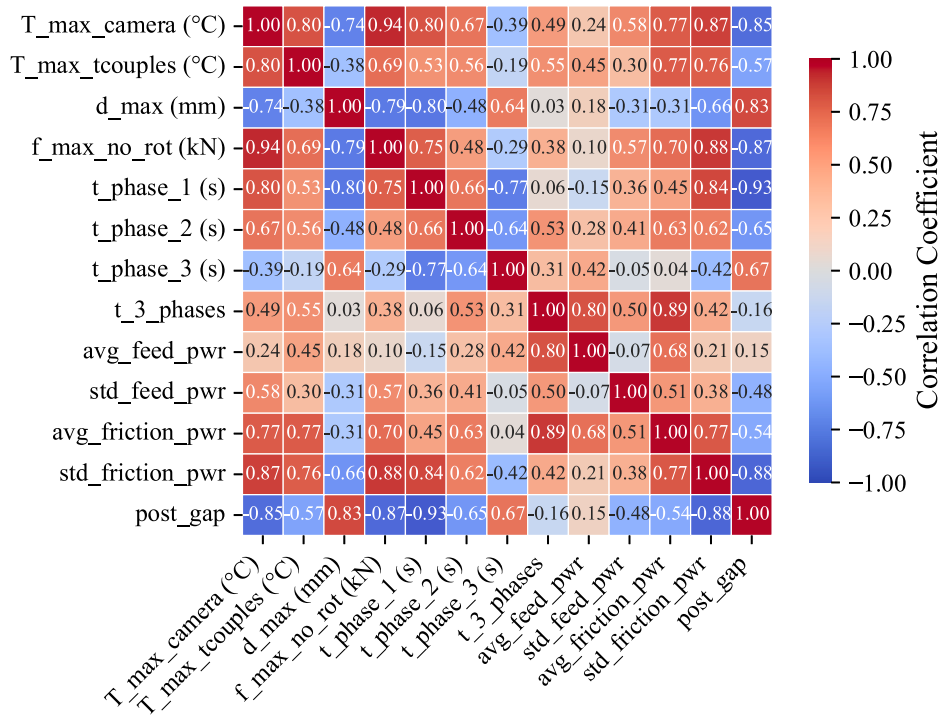


Fig. 10. Correlation matrix for the extracted features and the post-welding measured gap. Twelve samples with IG = {0, 0.2, 0.3, 0.4, 0.5, 0.6} mm were considered to build the correlation matrix.

during welding. As noted previously, such anomalies are inherent to the limitations of the use of thermocouples for monitoring this welding process. Instead, thermal imaging needs to maintain a clear view of the environment during acquisition. During the tests, unpredictable vibrations of the FEW machine or the camera may have altered the line of sight, which would explain the temperature drop of approximately 40 °C observed for IG0.3 at around 3.2 s.

2.3.4. Feature extraction and selection

Based on the previous discussions, the following features were extracted from the process and temperature acquisition signals: duration of penetration phase (t_{phase_1}), duration of cleaning phase

(t_{phase_2}), duration of welding phase (t_{phase_3}), total duration of the above 3 phases (t_{3_phases}), maximum element head displacement (d_{max}), axial force measured just before element rotation starts ($f_{max_no_rot}$), average and standard deviation of motors power signals (avg_feed_pwr , $avg_friction_pwr$, std_feed_pwr , $std_friction_pwr$), and maximum temperature recorded by both the IR camera and thermocouples (T_{max_camera} , $T_{max_tcouples}$).

It is worth remembering that the primary goal is to identify the post-welding gap (see Table 1), rather than to establish a direct relationship between the initial gap between sheets and the extracted features. Indeed, the process response to variations in initial gaps is not necessarily predictable, as certain conditions may change significantly.

Post-welding gaps were measured through macrographic examinations for 12 samples with IGs of {0, 0.2, 0.3, 0.4, 0.5, 0.6} mm. The range was limited to 0.6 mm, as observations indicated that the threshold between conforming and non-conforming post-welding gaps is between IG0.4 and IG0.6.

As shown in Fig. 1, this stage may involve a feedback loop known as *sensor selection*. To support this, Pearson correlation coefficients were calculated between the extracted features and the measured post-welding gaps, as

$$r = \frac{\sum_{i=1}^n (x_i - \bar{x})(y_i - \bar{y})}{\sqrt{\sum_{i=1}^n (x_i - \bar{x})^2} \sqrt{\sum_{i=1}^n (y_i - \bar{y})^2}}, \quad (1)$$

where n is the sample size, (x_i, y_i) are the individual feature values, and (\bar{x}, \bar{y}) are the feature means. The Pearson coefficient was selected for its suitability in measuring linear relationships.

Several features exhibit strong correlations (i.e., $|r| > 0.8$) with the post-welding gap, including maximum temperature from the IR camera (T_{max_camera}), maximum element head displacement (d_{max}), force just before element rotation begins ($f_{max_no_rot}$), penetration phase duration (t_{phase_1}), and the standard deviation of the friction motor ($std_friction_pur$). In contrast, the maximum temperature measured by thermocouples only shows a moderate correlation (-0.57), likely due to their high sensitivity to positioning errors. A moderate correlation can be observed for both std_feed_pur and $avg_friction_pur$, whereas phases sum, t_{3_phases} , and avg_feed_pur exhibit a low correlation. Notably, t_{phase_1} displays the strongest correlation with the post-welding gap and also correlates highly with T_{max_camera} (0.80) and with $std_friction_pur$ (0.84). Similarly, $f_{max_no_rot}$ has a strong correlation with T_{max_camera} (0.94), while d_{max} is closely related with both $f_{max_no_rot}$ and t_{phase_1} .

These findings demonstrate that penetration time, t_{phase_1} , and force just before element rotation starts, $f_{max_no_rot}$ emerge as the most informative predictors of the post-process gap.

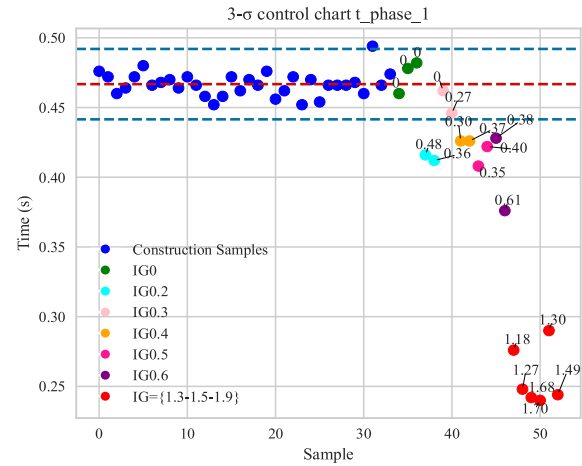
2.4. Decision support tool development and testing

The final stage of the proposed methodology involves the development and validation of a decision support tool. While data quantity could enable more complex approaches such as advanced data processing and machine learning (ML) methods, a more straightforward and interpretable solution is proposed here. Specifically, two $3\text{-}\sigma$ control charts [27] were developed using the most informative features identified earlier, i.e., t_{phase_1} and $f_{max_no_rot}$. Control limits for these charts were defined using 34 samples produced under benchmark conditions. Additional samples with varying IGs were then processed to evaluate the effectiveness of the control charts in detecting non-conforming welds.

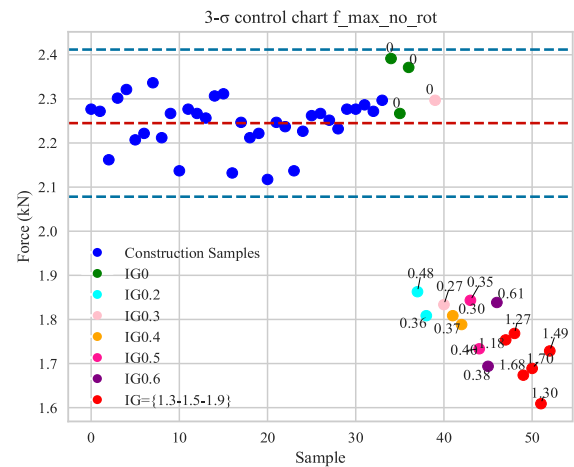
3. Results and discussion

Following the definition of the benchmark process, a series of welded samples was produced and examined through cross-sectional analysis to measure the post-welding gaps. Leveraging the correlation matrix shown in Fig. 10, the most informative features for identifying post-welding gaps were extracted, and two $3\text{-}\sigma$ limits control charts were constructed accordingly. Moreover, six additional samples with IGs of {1.3, 1.5, 1.9} mm were added to validate the proposed control charts.

Fig. 11 shows the resulting control charts. The first chart (Fig. 11(a)) is based on the duration of the penetration phase, while the second chart (Fig. 11(b)) tracks the force measured when the element rotation starts, at the onset of the penetration phase. Both charts show a general decreasing trend as the IG increases. As a consequence, this decreasing trend is associated with a corresponding increase in the post-welding gaps. This behavior results from the control mechanism based on



(a) Chart for penetration time.



(b) Chart for the force reached before element rotation in the penetration phase.

Fig. 11. $3\text{-}\sigma$ limits control charts for the selected features. The construction samples refer to the specimens made under benchmark process conditions and used to define the chart limits. The post-welding gap dimensions measured through macrographic examinations are indicated in mm next to each sample.

element head displacement. When an initial gap is present, the element can move downward more freely, since it initially only presses the upper sheet toward the lower one. Until the two sheets make contact, there is little resistance to the motion of the element. Consequently, especially in the presence of a large gap, the preset element head displacement of 1.8 mm, which drives the penetration phase, is achieved faster and with lower force. The time-related chart shows a higher sensitivity in detecting the extent of the post-welding gap. Samples with large IGs (i.e., {1.3, 1.5, 1.9} mm) are clearly differentiated from those with smaller IGs. Notably, in all cases where a post-welding gap is present, the force before element rotation consistently remains below 1.9 kN. This makes the $f_{max_no_rot}$ chart effective for detecting the presence of a post-welding gap, regardless of its extent.

Fig. 12 shows nine cross-sectional images of FEW joints, each representative of the effects of different IG values. The metallographic observations clearly demonstrate that the post-welding gap is strongly dependent on IG. For the IG0 condition, proper matching between the aluminum and steel sheets is achieved, with no detectable residual gap. This confirms that, in the absence of an initial gap, the FEW process ensures an optimal fit between the sheets, thereby minimizing the likelihood of post-welding separation. As the IG increases up to

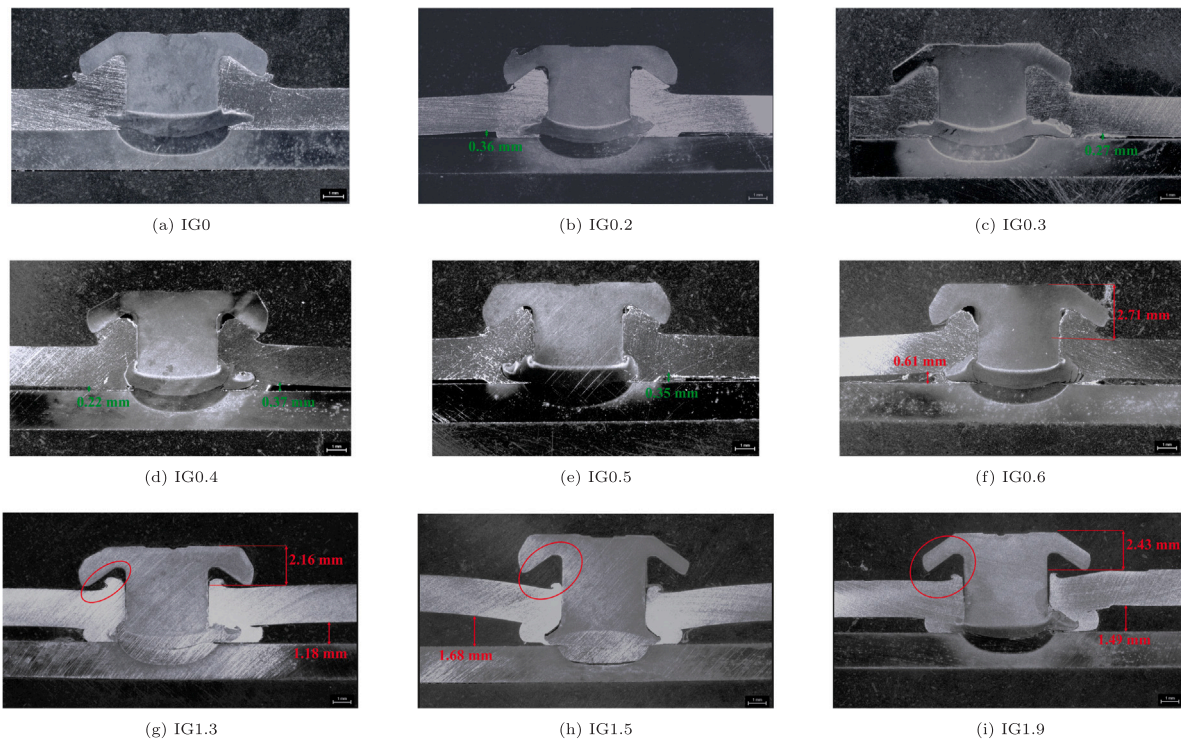


Fig. 12. Cross-sections for $IG = \{0.2, 0.3, 0.4, 0.5, 0.6, 1.3, 1.5, 1.9\}$ mm. The non-compliant features, as indicated in Table 1, are highlighted in red. (For interpretation of the references to color in this figure legend, the reader is referred to the web version of this article.)

0.5 mm, a progressive widening of the post-welding gap is observed; however, all the corresponding joints meet the quality requirements outlined in Table 1. In these conditions, the measured post-welding gaps range from 0.22 to 0.45 mm. Conversely, the IG0.6 condition exhibits borderline performance: in several cases, both the post-welding gap and element head criteria are not fulfilled (Fig. 12(f)), while in other instances compliance is maintained. Although Fig. 12 suggests a compliance limit of IG0.5, it is important to analyze the post-process gaps since the same IG could lead, due to uncontrolled factors, to a different result. For example, IG0.2 resulted in one sample really close to the compliance limit (post-gap = 0.48 mm) (see Fig. 11). At IGs over 0.6 mm, the degradation in joint quality is more pronounced. Under these conditions, the welds consistently fail to meet multiple requirements, particularly those concerning the element head and under-head filling (Figs. 12(g), 12(h), 12(i)). The analysis reveals a systematic relationship between the post-welding gap and other quality features of the FEW joints. Specifically, whenever the requirements for under-head filling and element head distance are not met, the post-welding gap requirement is also not satisfied. Conversely, compliance with the post-welding gap requirement reliably ensures that all other quality criteria are fulfilled. Under the examined conditions, the findings indicate that the post-welding gap requirement is the most conservative requirement for identifying non-conforming FEW joints. Therefore, larger initial gaps not only limit sheet matching close to the FEW joint but also undermine the overall weld integrity.

Overall, the proposed control charts are effective in identifying post-welding gaps. Specifically, penetration time proves to be a reliable indicator for detecting gaps exceeding the acceptable threshold, provided that appropriate control limits are established. Furthermore, these control charts serve as a valuable tool for real-time process monitoring, enabling the early detection of undesirable shifts or deviations during the FEW process.

4. Conclusion

This study proposes a domain-knowledge-based framework for quality monitoring in FEW, applied to the welding of 6xxx aluminum alloy

and *Usibor*[®] 2000 steel for automotive applications. The approach involves process analysis, definition of quality requirements, identification of measurable quantities, and sensor system implementation. The experimental campaign addressed both the benchmark process and the influence of initial gaps between the sheets as a process disturbance. Features extracted from the process signals, an IR thermal camera, and thermocouples were analyzed and correlated with the resulting post-welding gap, leading to the identification of the most relevant indicators through three-limits control charts for real-time quality monitoring. Key findings are as follows:

- The penetration phase duration and the axial force measured just before element rotation starts are identified as the features most strongly correlated with the post-process gap.
- Peak temperatures during welding are highly informative for monitoring FEW quality, with increasing IGs correlating to reduced peak temperatures. Importantly, peak temperatures correlate strongly with process signals. Since direct temperature measurement could be cost-prohibitive and often impractical in large-scale production, process signals may offer a feasible alternative for quality assessment.
- The proposed control charts, based on penetration time and the axial force just before element rotation starts, are effective in identifying post-welding gaps. As such, they serve as practical tools for FEW process monitoring and for identifying defective welds in real-time.

Overall, the proposed approach can serve as a basis for developing more advanced quality monitoring tools for FEW. In the context of Industry 5.0, which emphasizes human-machine collaboration, operators require accessible and user-friendly decision-support systems. Simple tools such as control charts, though well-established, continue to meet modern industrial needs and have regained relevance. While advanced approaches like machine learning can be powerful, they require large, structured datasets that are often unavailable from production lines. In contrast, simple and interpretable tools, like those proposed in this

study, remain robust under limited data availability and offer practical, easily applicable solutions. The proposed framework could also support domain-knowledge-based ML models, enabling further research on automated defect detection during the quality specification phase.

To conclude, because this work is limited to uniform IG, future implementation could focus on testing the proposed approach under other non-ideal conditions, such as the presence of a non-uniform or one-sided gap.

CRedit authorship contribution statement

Gabriel Antal: Writing – review & editing, Writing – original draft, Validation, Methodology, Investigation, Formal analysis, Data curation. **Valentino Razza:** Writing – review & editing, Writing – original draft, Validation, Methodology, Investigation, Formal analysis, Data curation. **Pasquale Russo Spena:** Writing – review & editing, Writing – original draft, Validation, Supervision, Methodology, Investigation, Conceptualization. **Manuela De Maddis:** Writing – review & editing, Writing – original draft, Validation, Supervision, Methodology, Investigation, Conceptualization.

Declaration of competing interest

The authors declare that they have no known competing financial interests or personal relationships that could have appeared to influence the work reported in this paper.

Acknowledgments

This research was supported by the project MANAGE 5.0 F/310302/01-05/X56 (MANufacturing Automotive Green Evolution 5.0). The authors express their gratitude to their academic supervisor, Prof. Franco Lombardi (Politecnico di Torino), for his guidance. They also wish to thank Antonio Annicchiarico (Stellantis), Alessandro Cacciato (Stellantis), Massimo Di Pardo (Stellantis), and Matteo Perrone (Politecnico di Torino), for their support during the experimental campaign and helpful discussions.

References

- Meschut G, Janzen V, Olfermann T. Innovative and highly productive joining technologies for multi-material lightweight car body structures. *J Mater Eng Perform* 2014;23(5):1515–23. <http://dx.doi.org/10.1007/s11665-014-0962-3>.
- Abankar M, De Maddis M, Razza V, Russo Spena P. Resistance element welding (REW) of steels with non-ferrous materials: Potentials, challenges, and properties. *Metals* 2024;14(12). <http://dx.doi.org/10.3390/met14121448>.
- Sun Y, Huang R, Zhao H, Chen X, Jiang M, Wu L, et al. Enhancement of resistance element welding of AA6061 to DP600 steel by using external magnetic field. *J Manuf Process* 2022;80:347–58. <http://dx.doi.org/10.1016/j.jmapro.2022.06.001>.
- Martinsen K, Hu S, Carlson B. Joining of dissimilar materials. *CIRP Ann - Manuf Technol* 2015;64(2):679–99. <http://dx.doi.org/10.1016/j.cirp.2015.05.006>.
- Ding C, Xiao J, Gai S, Chen S. Electrode-embedded linear actuating enhanced resistance spot welding of aluminium alloy and dual phase steel. *J Manuf Process* 2024;132:811–23. <http://dx.doi.org/10.1016/j.jmapro.2024.11.038>.
- Shi L, Carlson BE, Li S, Ghassemi-Armaki H, Li G. Strengthening mechanism of aluminum weld nugget in novel dissimilar resistance spot welds of AA5754 to steels. *J Mater Eng Perform* 2025. <http://dx.doi.org/10.1007/s11665-025-10956-6>.
- Deng L, Lou M, Li Y, Carlson BE. Thermally assisted self-piercing riveting of AA6061-T6 to ultrahigh strength steel. *J Manuf Sci Eng Trans the ASME* 2019;141(10). <http://dx.doi.org/10.1115/1.4044255>.
- Wang R, Xiao P, Li H, Song H, Lu H, Zhang Y, et al. Development of remarkable fatigue properties of self piercing riveting of HC950/1300HS and AA6082-T6 with conventional rivet. *J Mater Res Technol* 2025;35:853–7. <http://dx.doi.org/10.1016/j.jmrt.2025.01.081>.
- Fei L, Feng Z, Jiang F, Zhang Y, Zhao S. Process optimization of robust bonding between DP590 and AA6061 using resistance riveting welding. *J Manuf Process* 2023;104:273–88. <http://dx.doi.org/10.1016/j.jmapro.2023.09.004>.
- Niu S, Wang Z, Lou M, Ma Y, Lei H, Li Y. Resistance rivet welding of aluminum/titanium dissimilar materials. *J Manuf Process* 2023;108:141–52. <http://dx.doi.org/10.1016/j.jmapro.2023.10.051>.
- Niu S, Ma Y, Lou M, Zhang C, Li Y. Joint formation mechanism and performance of resistance rivet welding (RRW) for aluminum alloy and press hardened steel. *J Mater Process Technol* 2020;286. <http://dx.doi.org/10.1016/j.jmatprot.2020.116830>.
- Meschut G, Hahn O, Janzen V, Olfermann T. Innovative joining technologies for multi-material structures. *Weld the World* 2014;58(1):65–75. <http://dx.doi.org/10.1007/s40194-013-0098-3>.
- Wu J, Chen C, Ouyang Y, Qin D, Li H. Recent development of the novel riveting processes. *Int J Adv Manuf Technol* 2021;117(1–2):19–47. <http://dx.doi.org/10.1007/s00170-021-07689-w>.
- Meschut G, Schmal C, Olfermann T. Process characteristics and load-bearing capacities of joints welded with elements for the application in multi-material design. *Weld the World* 2017;61(3):435–42. <http://dx.doi.org/10.1007/s40194-017-0431-3>.
- Skovron JD, Ruszkiewicz BJ, Mears L, Abke T, Varma A, Li Y, et al. Investigation of the cleaning and welding steps from the friction element welding process. In: International manufacturing science and engineering conference. Processes, Vol. 1, 2017. <http://dx.doi.org/10.1115/MSEC2017-2786>.
- Ruszkiewicz BJ, Skovron JD, Absar S, Choi H, Zhao X, Mears L, et al. Parameter sensitivity and process time reduction for friction element welding of 6061-T6 aluminum to 1500 MPa press-hardened steel. *SAE Int J Mater Manuf* 2018;12(1):41–56. <http://dx.doi.org/10.4271/05-12-01-0004>.
- Awate G, Mahajan NN, Choi H. Investigating the effects of SiC abrasive particles on friction element welding. *Manuf Lett* 2022;33:259–71. <http://dx.doi.org/10.1016/j.mfglet.2022.07.034>.
- Deshpande AB, Grimm TJ, Mears L. Chipping reduction using thermally-assisted friction element welding. In: Proceedings of the ASME 2021 16th international manufacturing science and engineering conference, vol. 2. 2021. <http://dx.doi.org/10.1115/MSEC2021-61180>.
- Grimm TJ, Parvathy GV, Mears L. Laser-assisted friction element welding. In: ASME international mechanical engineering congress and exposition, proceedings, vol. 2A-2021. 2021. <http://dx.doi.org/10.1115/IMECE2021-69029>.
- Grimm TJ, Parvathy GV, Mears L. Resistance heat assisted friction element welding. In: ASME international mechanical engineering congress and exposition, proceedings, vol. 2A-2021. 2021. <http://dx.doi.org/10.1115/IMECE2021-68747>.
- Varma A, Absar S, Ruszkiewicz BJ, Skovron JD, Mears L, Choi H, et al. Numerical study of temperature evolution during friction element welding. *J Manuf Sci Eng* 2022;144(12). <http://dx.doi.org/10.1115/1.4055164>.
- Varma A, Nassiri A, Mears L, Choi H, Zhao X. Numerical study of chipping during friction element welding. *Manuf Lett* 2022;34:75–7. <http://dx.doi.org/10.1016/j.mfglet.2022.09.007>.
- Absar S, Ruszkiewicz BJ, Skovron JD, Mears L, Abke T, Zhao X, et al. Temperature measurement in friction element welding process with micro thin film thermocouples. *Procedia Manuf* 2018;26:485–94. <http://dx.doi.org/10.1016/j.promfg.2018.07.057>.
- Mishra D, Roy RB, Dutta S, Pal SK, Chakravarty D. A review on sensor based monitoring and control of friction stir welding process and a roadmap to Industry 4.0. *J Manuf Process* 2018;36:373–97. <http://dx.doi.org/10.1016/j.jmapro.2018.10.016>.
- Stellantis - Partner of the project MANAGE50. Personal communication. 2024.
- EJOT Group. 2025. URL <https://www.ejot.com/>. [Accessed 21 August 2025].
- Yang J, Xie M, Goh TN. Control limits based on the narrowest confidence interval. *Comm Statist Theory Methods* 2011;40(12):2172–81. <http://dx.doi.org/10.1080/03610921003746685>.